(Received 1 October 2025, Accepted 13 November 2025, Scheduled 20 November 2025)

A Compact Four-Port Axially Symmetric UWB-MIMO Antenna Array: Metamaterial-Integrated Coplanar Waveguide for Broadband Operation with High Isolation

Xuemei Zheng[1], Linfei Yue[2,*], and Yunan Zhang[2]

[1] *Key Laboratory of Modern Power System Simulation and Control and Renewable Energy Technology, Ministry of Education, Northeast Electric Power University, Jilin, China*
[2] *School of Electrical Engineering, Northeast Electric Power University, Jilin, China*

ABSTRACT: This paper presents a broadband MIMO antenna for miniaturized satellites and a novel metamaterial for decoupling. The proposed metamaterial exhibits single-negative characteristics (with only permittivity ε being negative) in the 4.66–6 GHz and 6.5–9 GHz frequency bands, and double-negative characteristics (with both permittivity ε and permeability μ being negative) in the 6–6.5 GHz and 9–15.97 GHz frequency bands. In MIMO antenna applications, it significantly improves isolation between antenna elements. Finally, we develop a 4-port ultra-wideband (UWB) MIMO array antenna operating from 4.66 to 15.97 GHz, covering C-band, X-band, and Ku-band. It achieves $S_{11} < -10$ dB with an operating bandwidth of 11.31 GHz. With the integrated metamaterial suppressing inter-unit coupling, the antenna demonstrates low-coupling performance (S_{12}, S_{13}, $S_{14} < -20$ dB and ECC < 0.035) across the entire operating band. The maximum gain reaches 7.83 dBi, providing both high-gain performance and ultra-wideband decoupling capabilities. This MIMO antenna measures 55 mm $\times$ 55 mm $\times$ 1.6 mm and uses an FR4 substrate.

1. INTRODUCTION

Recent years have witnessed extensive deployment of 5G communication systems [1] and rapid advancement in 6G research. Wireless communication systems across various application scenarios now demand increasingly rigorous antenna performance requirements. They include operating bandwidth, gain, miniaturization, omnidirectional radiation characteristics, and isolation. Ultra-wideband (UWB) multiple-input multiple-output (MIMO) antennas [2, 3] have emerged as viable solutions to these demands. However, such antennas face new challenges. The highly compact integration of antenna elements induces severe electromagnetic coupling between adjacent elements. Consequently, addressing electromagnetic coupling in UWB MIMO antennas and achieving effective antenna miniaturization have become urgent research priorities.

Numerous scholars have proposed various decoupling methodologies for UWB MIMO antennas. Ref. [4] designs a 2-port UWB antenna configuration with two radiating elements measuring $85 \times 45\,\text{mm}^2$. Each element adopts a coplanar waveguide (CPW)-fed rectangular patch design with double U-shaped slots etched on patches to introduce dual notch features. However, this antenna exhibits excessive dimensions, failing to comply with miniaturization design paradigms. Furthermore, the design does not adequately address electromagnetic coupling between antenna elements, resulting in prominent inter-element coupling issues. Ref. [5] proposes a 4-port MIMO antenna integrated with a split-ring resonator (SRR) metamaterial layer to enhance antenna gain. Unfortunately, this antenna occupies $140 \times 70\,\text{mm}^2$, failing miniaturization criteria, and suffers from significant inter-element coupling.

Ref. [6] presents two microstrip line-fed pentagonal patches with parasitic elements to achieve wide bandwidth. Simultaneously, three complementary split-ring resonator (CSRR) structures were integrated into a defected ground structure to mitigate mutual coupling. Unfortunately, these structures severely impact the radiation pattern, leading to poor antenna radiation directivity. Ref. [7] proposes chamfering radiating patches and adding parasitic patches for miniaturization. A double-layer metamaterial decoupling structure (comprising an open resonant ring and a square ring) was loaded above the elements for decoupling. However, this antenna operates only from 12.11 to 13.99 GHz, which is excessively narrow. Additionally, its double-layer structure makes it incompatible with ultra-thin devices, limiting application scenarios.

Ref. [11] proposes an 8-port CPW-fed UWB MIMO antenna measuring $54 \times 54\,\text{mm}^2$. However, its isolation is only -15 dB, requiring enhanced decoupling. Ref. [12] proposes a 2-port monopole UWB antenna for modern automotive applications, composed of a half-circular ring and a half-square ring. However, its isolation is only -15 dB, necessitating further decoupling enhancement. Meanwhile, a 4-port design could be considered. Ref. [13] proposes a compact asymmetric CPW strip-fed UWB two-element MIMO antenna with notched-band behavior. This antenna has a simple structure and is easy to fabri-

* Corresponding author: Linfei Yue (2202400422@neepu.edu.cn).

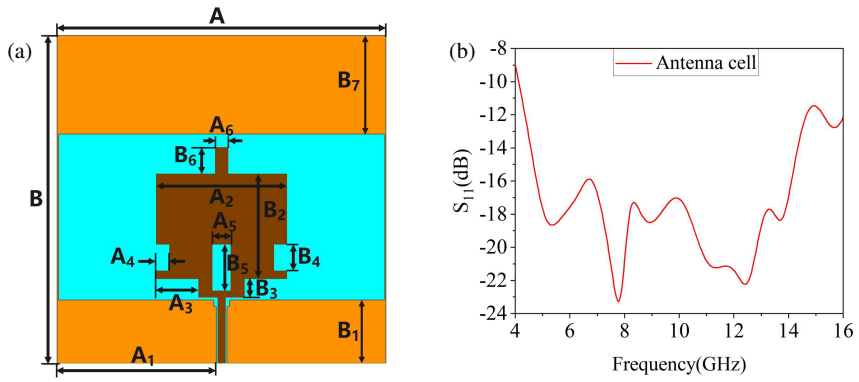

FIGURE 1. Antenna cell design: (a) Antenna cell planar parameter diagram; (b) S-parameters of antenna cell.

cate. However, it suffers from low gain and lacks comprehensive performance analysis.

Ref. [14] proposes an eight-element antenna array. However, this antenna has narrow bandwidth and low isolation, resulting in limited application scenarios. Ref. [15] proposes a 2-port MIMO antenna array with a compact size of $26 \times 55\,\text{mm}^2$, operating from 3.1 to 12.3 GHz. However, the antenna achieves only 4 dBi gain, failing to meet long-distance communication requirements. Ref. [16] proposes a 2-port MIMO antenna array composed of two symmetric C-shaped slots and T-shaped slots. The isolation between antenna elements exceeds 18 dB. However, the operating frequency band is only 2.4–4.5 GHz, and gain discussion is lacking. Ref. [17] proposes a 2-port MIMO antenna array measuring $38 \times 91\,\text{mm}^2$, operating from 2.8 to 10.0 GHz. However, this antenna has a relatively complex structure, and its radiation pattern fails to meet omnidirectionality requirements. Ref. [18] proposes a new method for mask-constrained shaped beam synthesis of generic array antennas (arbitrary layouts/patterns). This method transforms the design into finite convex programming optimizations (generating qualified excitation solutions) and is supported by numerical examples.

Based on this analysis, this paper proposes using a CPW structure to address antenna operating bandwidth issues. This enables UWB operation while leveraging inherent structural advantages to achieve high antenna gain and omnidirectional radiation performance. We also propose a metamaterial [8] capable of UWB decoupling to ensure high antenna isolation across the entire operating spectrum. Ultimately, we design a 4-port array MIMO antenna based on the proposed metamaterial. It features an operating frequency range of 4.12–16.58 GHz, a bandwidth of 12.46 GHz, and a relative bandwidth of 120%. The antenna exhibits high isolation performance, with S_{12}, S_{13}, and $S_{14} < -20$ dB across the full frequency band. Owing to its single-layer substrate structure and ultra-wide operating bandwidth, this antenna holds considerable engineering application potential. Finally, we conducted experimental tests on the antenna prototype. The results demonstrate excellent consistency between simulated and measured performances.

2. ANTENNA AND METAMATERIAL DESIGN

This section describes the structural designs of a CPW-structured UWB antenna element, a metamaterial capable of ultra-wideband decoupling, and a four-port, axisymmetric, compact UWB-MIMO antenna integrated with the aforementioned metamaterial.

2.1. Antenna Cell Design and Analysis

Figure 1 shows the antenna unit based on a classical coplanar waveguide structure. It features openings and notches in the radiating patch and recesses in the transmission line. The antenna unit bandwidth spans 4.12–16.58 GHz. The unit demonstrates good impedance matching with $S_{11} < -15$ dB from 4.67 to 14.22 GHz.

We performed modeling and simulation using High Frequency Structure Simulator (HFSS) software. The final antenna unit size is 25 mm × 25 mm × 1.6 mm. Table 1 shows specific structural parameters. The antenna is printed on an FR4 dielectric substrate (dielectric constant of 4.4, dielectric loss tangent of 0.02).

TABLE 1. Dimensions of the optimized antenna structure (unit: mm).

Parameters	Dimensions (mm)	Parameters	Dimensions (mm)
A	25	B	25
A_1	12.1	B_1	4.8
A_2	10	B_2	8.1
A_3	3.22	B_3	1.4
A_4	1	B_4	2
A_5	1.4	B_5	3.5
A_6	1	B_6	2
H	1.6	B_7	7.5

2.2. Metamaterial Unit Design and Analysis

From the perspective of metamaterial working principles, metamaterials can effectively suppress surface wave propagation and reduce cell edge scattering [9, 19]. This significantly improves radiation efficiency and reduces mutual coupling effects. In this paper, the metamaterial-loaded decoupling structure achieves high isolation below −20 dB in an ultra-wide frequency band (4.66–15.97 GHz) through inverse coupling path cancellation. This solves the problem of high-frequency band coupling deterioration in traditional antennas.

We modeled and simulated the metamaterial using HFSS simulation software. In the simulation, we set the left and right

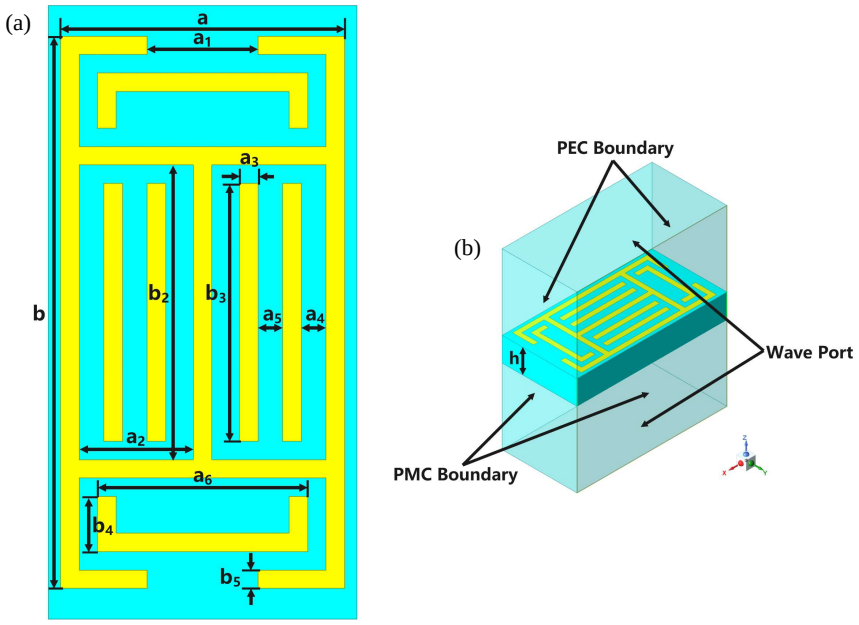

FIGURE 2. Metamaterial unit design: (a) Metamaterial unit planar parameter diagram; (b) Metamaterial unit 3D structure diagram.

surfaces perpendicular to the z-axis as wave port excitations. The top and bottom surfaces perpendicular to the y-axis were set as ideal magnetic conductors (Perfect H). The front and back surfaces perpendicular to the x-axis were set as ideal electric conductors (Perfect E). The magnetic field is perpendicular to the metamaterial cell surface to simulate magnetic resonance generation when the magnetic field passes through the cell. Figure 2 and Table 2 show the structure and specific parameters.

TABLE 2. Dimensions of the optimized metamaterial structure (unit: mm).

Parameters	Dimensions (mm)	Parameters	Dimensions (mm)
a	4.6	b	9
a_1	1.8	b_1	1.5
a_2	1.85	b_2	4.8
a_3	0.3	b_3	4.2
a_4	0.4	b_4	0.9
a_5	0.4	b_5	0.3
a_6	3.4	h	1.6

This paper uses the widely adopted waveguide simulation method for electromagnetic parameter extraction. Figure 3 shows the S_{11} and S_{21} parameters of the metamaterial obtained from HFSS simulation. The figure reveals that the metamaterial has large transmission attenuation from 6–10 GHz and 12–20 GHz. This indicates band-resistive properties in these frequency ranges.

To further obtain equivalent electromagnetic parameters, we introduce the Nicolson-Ross-Weir (NRW) method [10, 20] to extract the antenna's equivalent electromagnetic parameters. The theoretical calculations involve S-parameter extraction technique as follows: S_{11} denotes the reflection coefficient. The relationship between S_{12} and transmission coefficient T

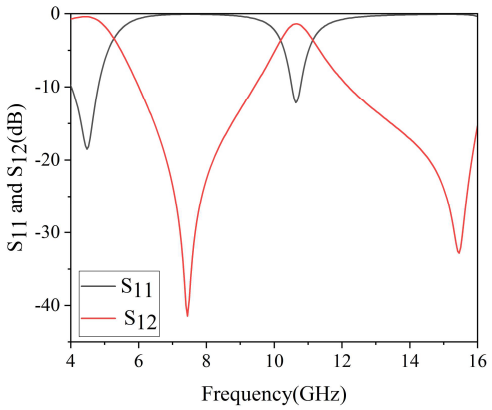

FIGURE 3. S-parameters of metamaterial unit.

can be expressed as:

$$S_{21} = Te^{ik_0 d}, \tag{1}$$

where k_0 denotes the wave number of the incident wave in free space, and d denotes the thickness of the uniform medium plate. Furthermore, the relationship between the S-parameter and the refractive index n and impedance z can be expressed as:

$$S_{11} = \frac{R_{01}\left(1 - e^{i2nk_0 d}\right)}{1 - R_{01}^2 e^{i2nk_0 d}}, \tag{2}$$

$$S_{21} = \frac{\left(1 - R_{01}^2\right) e^{ink_0 d}}{1 - R_{01}^2 e^{i2nk_0 d}}, \tag{3}$$

$$R_{01} = (z-1)/(z+1). \tag{4}$$

We can obtain the expression for impedance z from Equations (2) and (3):

$$Z = \pm\sqrt{\frac{(1+S_{11})^2 - S_{21}^2}{(1-S_{11})^2 - S_{21}^2}}, \tag{5}$$

$$e^{ink_0d} = X \pm i\sqrt{1-X^2}, \tag{6}$$

$$X = 1/2\left[S_{21}\left(1 - S_{11}^2 + S_{21}^2\right)\right]. \tag{7}$$

Since the metamaterial under consideration is a passive medium, z and n in the equations need to satisfy the following conditions:

$$\mathrm{Re}(z) \geq 0, \tag{8}$$

$$\mathrm{Im}(n) \geq 0, \tag{9}$$

the formula for finding the refractive index n value is:

$$n = \frac{1}{k_0 d}\left\{\left[\mathrm{Im}[\mathrm{In}(e^{ink_0d})] + 2m\pi\right] - i\mathrm{Re}\left[\mathrm{In}(e^{ink_0d})\right]\right\}, \tag{10}$$

where m is an integer associated with $\mathrm{Re}(n)$. Finally, we can obtain two parameters that determine metamaterial properties from these two equations. Magnetic permeability and dielectric constant are, respectively,

$$\mu = n \times z, \tag{11}$$

$$\varepsilon = n/z. \tag{12}$$

Figure 4 shows the extracted equivalent parameter results based on the above theory.

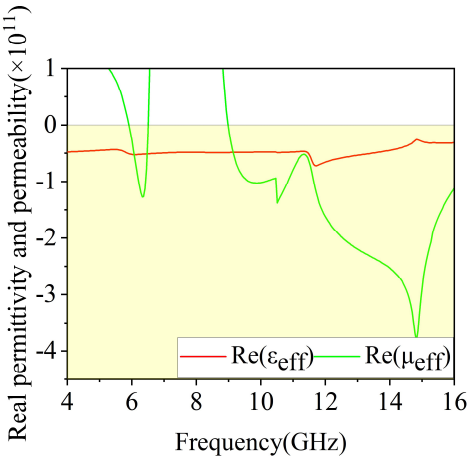

FIGURE 4. Plot of the extracted equivalent parameter values.

Figure 4 presents the curves of equivalent permittivity and equivalent permeability (extracted via waveguide simulation) as functions of frequency. The figure shows that the proposed novel metamaterial behaves as an epsilon-negative (ENG) metamaterial with negative permittivity ($\varepsilon < 0$) but positive permeability ($\mu > 0$) in the 4.66–6 GHz and 6.5–9 GHz frequency bands, and as a double-negative (DNG) metamaterial with both negative permittivity ($\varepsilon < 0$) and negative permeability ($\mu < 0$) in the 6–6.5 GHz and 9–15.97 GHz frequency bands.

2.3. UWB-MIMO Antenna Design and Analysis

The MIMO antenna design begins with antenna units placed in a centrosymmetric arrangement. We first designed Antenna 1, but its impedance matching and bandwidth deteriorated. Therefore, we designed Antenna 2 by digging a slot in the center of the antenna array based on Antenna 1. Antenna 2 shows improvements in impedance matching and antenna isolation. On Antenna 2, we introduced branches using the traditional ultra-wideband decoupling approach to achieve low coupling. However, due to high integration and antenna coplanar waveguide structure, good decoupling effect remains unachieved.

Based on these experimental results, the designed Antenna 3 adopts a novel metamaterial approach to achieve good impedance matching and low-coupling ultra-wideband effect. We performed simulation of each antenna using HFSS simulation software. Figure 5 shows the simulation results and specific design process.

The experimental results show that the metamaterial-loaded MIMO antenna achieves an ultra-wideband 4.66–15.97 GHz operating band, indicating good impedance matching. We also observe that the S_{12}, S_{13}, and S_{14} parameters are all < -20 dB, confirming the modified antenna's low coupling characteristics. Therefore, subsequent discussion will focus on the loaded metamaterial Antenna 3.

3. OVERALL BROADBAND MIMO ANTENNA STRUCTURE DESIGN PROCESS AND RESULT ANALYSIS

3.1. MIMO Antenna Structure Design Process

Figure 6 and Table 3 show the finalized MIMO antenna structure and specific parameters. The left side of Figure 6 shows the antenna front view, while the right side shows the back view. This antenna features a coplanar waveguide structure. The top layer contains four radiating patch antenna units and metamaterials. The radiating patch and ground plate are located in the same top layer. We placed radiating patches to realize spatial orthogonal polarization, aiming to achieve low coupling while minimizing volume. We also placed metamaterials in the antenna's bottom layer. The two metamaterial layers further reduce antenna coupling. Therefore, the antenna's back side also features metamaterials, obtained by folding the front-side metamaterials by 180°.

TABLE 3. MIMO antenna structure parameters (unit: mm).

Parameters	Dimensions (mm)	Parameters	Dimensions (mm)
L	55	L_3	0.7
W_1	5	L_4	1
L_1	17	W_2	1.2
L_2	1.2	h	1.6

3.2. S-Parameter Simulation Analysis

This subsection investigates the influence of antenna element spacing on mutual coupling and isolation performance under

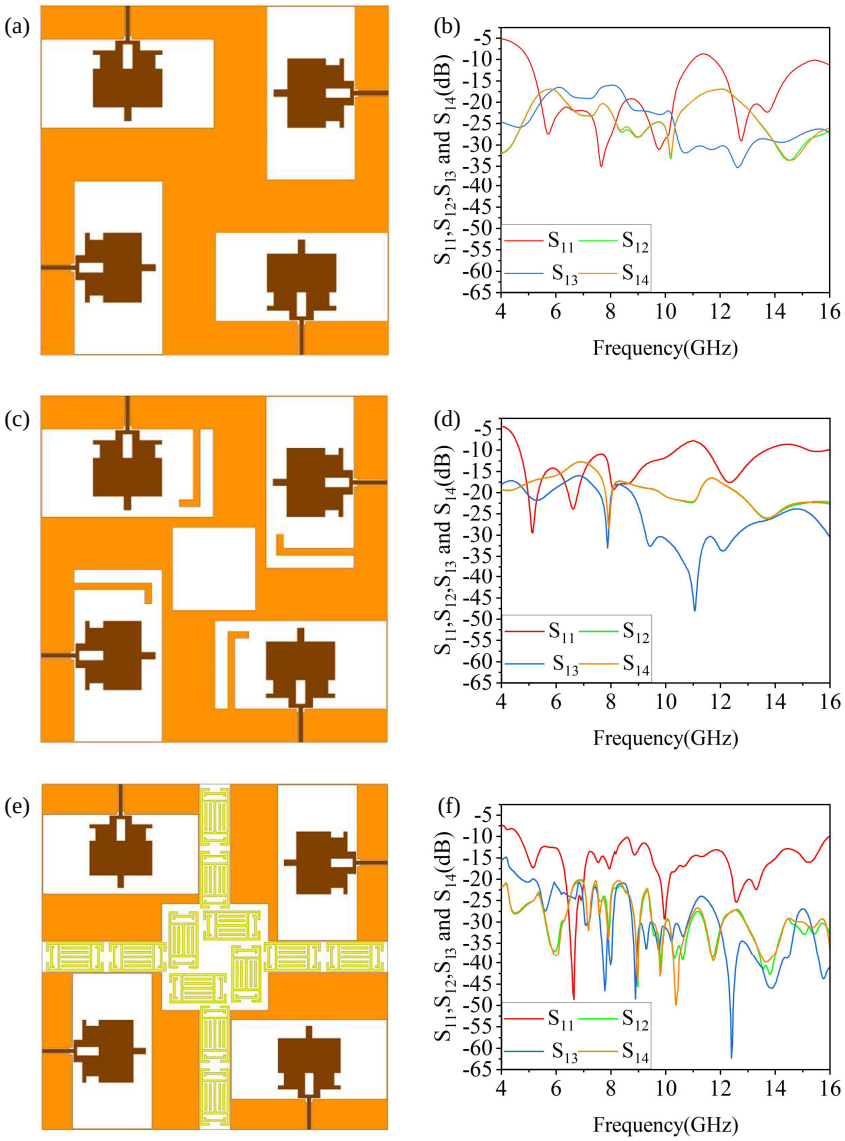

FIGURE 5. MIMO antenna design steps and comparison of S-parameters of three kinds of antennas: (a) Initial MIMO Antenna 1; (b) S-parameters of initial MIMO antenna; (c) Add branch MIMO Antenna 2; (d) S-parameters of add branch MIMO antenna; (e) Add metamaterial MIMO Antenna 3; (f) S-parameters of add metamaterial MIMO antenna.

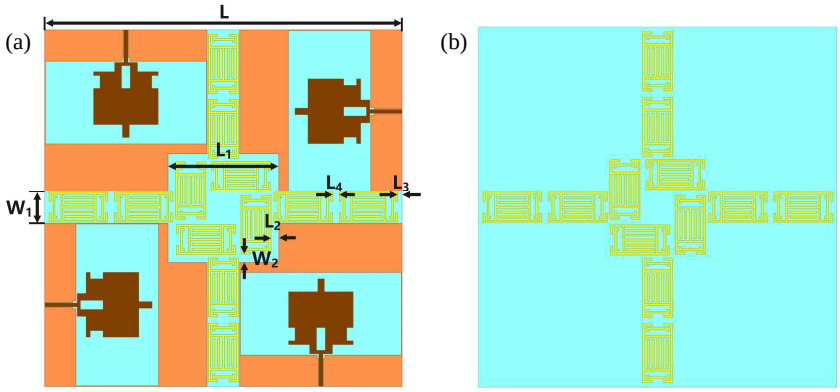

FIGURE 6. MIMO antenna structure: (a) MIMO antenna above parameter diagram; (b) MIMO antenna bottom diagram.

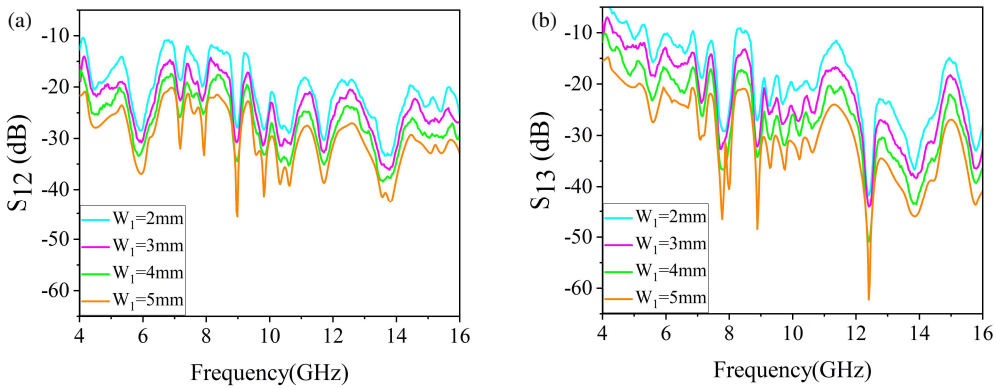

FIGURE 7. Comparison diagram of S-parameters: (a) S_{12}; (b) S_{13}.

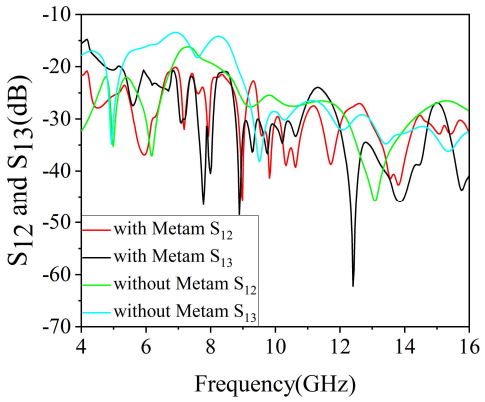

FIGURE 8. Comparison diagram of S-parameters (with and without metamaterial).

metamaterial loading conditions. We compared simulation results for four values of parameter W_1 (2 mm, 3 mm, 4 mm, and 5 mm), as shown in Figure 7. We found that larger antenna element spacing improves mutual coupling and isolation performance. However, considering antenna miniaturization requirements, we finally determined $W_1 = 5$ mm. All subsequent discussions assume $W_1 = 5$ mm.

To visualize the new decoupling structure's effect and considering MIMO antenna characteristics, we note that S_{12} and S_{14} are identical curves. Therefore, when comparing decoupling effect before and after metamaterial loading, we only need to compare S_{12} and S_{13}. Figure 8 shows S_{12} and S_{13} curve comparisons before and after metamaterial hybrid decoupling loading based on HFSS simulation. The figure shows that after loading the metamaterial hybrid decoupling structure, antenna isolation improves overall. Decoupling characteristics significantly improve across most of the antenna's operating frequency range. Specifically, S_{12} and S_{13} isolation reaches less than -27 dB from 11.73–15.97 GHz, achieving high isolation. The biggest improvements occur at 5.85, 8.2, and 8.65 GHz, with 12, 20, and 17 dB improvements, respectively. Even in the low-frequency band, metamaterials maintain antenna isolation below -20 dB. Therefore, the antenna achieves low-coupling working characteristics across the entire frequency band, fully demonstrating the new decoupling structure's effectiveness.

3.3. Analysis of Decoupling Characteristics of Metamaterials

This subsection discusses the antenna's decoupling mechanism [21]. First, we analyze the decoupling scheme with metamaterial integrated on the antenna's top layer. Simulation results show that top-layer metamaterial integration achieves certain decoupling effect. However, S_{12}, S_{13}, and S_{14} values only reach less than -15 dB, failing to meet design requirements. Therefore, we integrated a second metamaterial layer on the antenna's bottom layer. Simulation results show that with both top and bottom metamaterial layers integrated, S_{12}, S_{13}, and S_{14} values all reach less than -20 dB. The minimum value reaches -65 dB at 12.4 GHz, exhibiting excellent decoupling effect. Hence, this design adopts metamaterial integration on both top and bottom layers to realize MIMO antenna decoupling, as shown in Figure 9.

The physical significance of using metamaterials on both layers is as follows: the top-layer metamaterial mainly intercepts antenna plane waves through its band-stop characteristic, reducing the coupling between antenna elements and improving isolation. However, single-layer metamaterial decoupling effect is limited. Therefore, integrating metamaterials on both layers enhances the band-stop characteristic, strengthens decoupling effect, and thus achieves favorable decoupling performance.

3.4. MIMO Antenna Radiation Direction Diagram

To more intuitively analyze antenna far-field radiation characteristics, we select E-plane and H-plane patterns for analysis (black lines indicate E-plane patterns, red lines indicate H-plane patterns). We analyze patterns at four frequency points: 5.1 GHz, 6.84 GHz, 10 GHz, and 12.6 GHz. Figure 10 shows simulated patterns, revealing omnidirectional radiation characteristics at all four frequency points. At 5.1 GHz, there is a depression at 90°. At 7.18 GHz and 8.94 GHz, there are depressions at 270°, but they do not affect overall omnidirectional characteristics. As frequency increases, the antenna radiation pattern exhibits distortion at 12.6 GHz. This mainly results from higher-order mode resonance excitation at high frequencies, leading to uneven current density distribution on the antenna. However, this characteristic still meets engineering requirements.

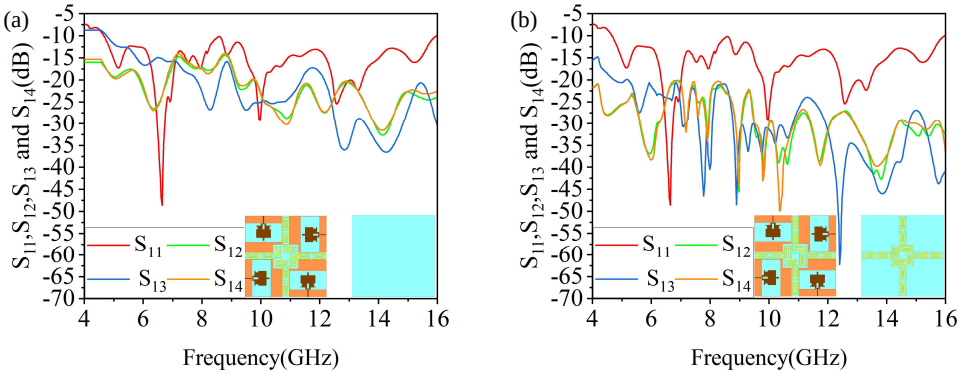

FIGURE 9. Antenna with metamaterial integrated only on the top layer and both the top and bottom layers: (a) Only on the top layer; (b) Both the top and bottom layers.

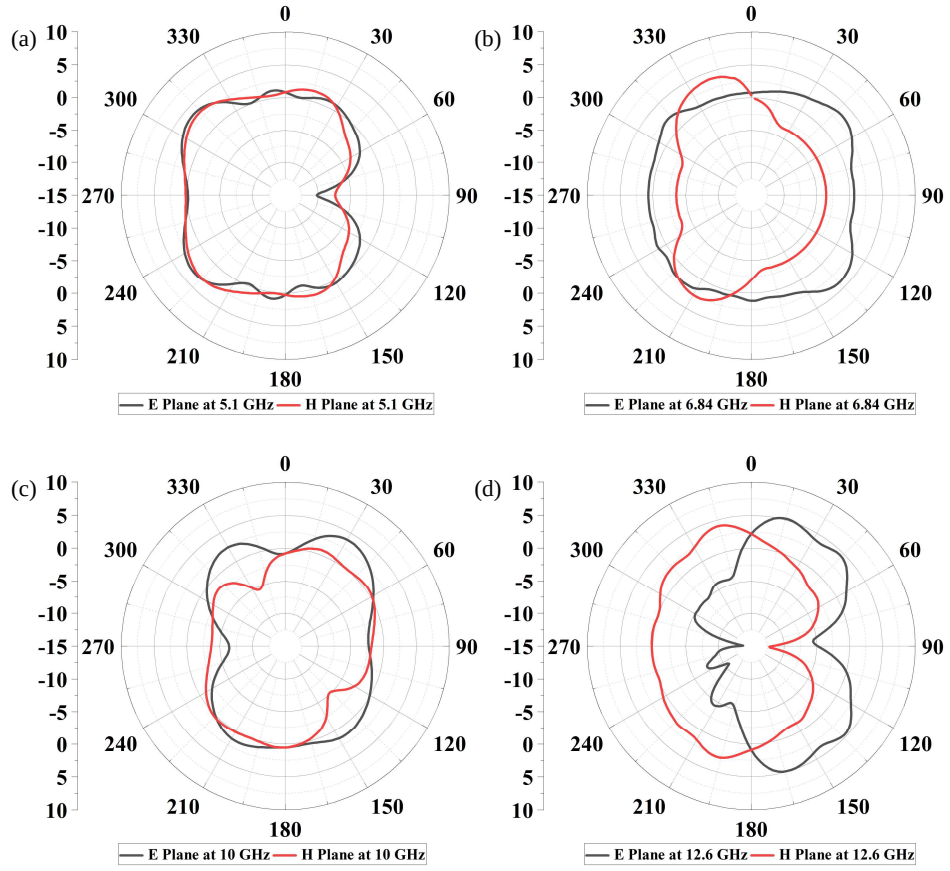

FIGURE 10. Radiation patterns of the antenna: (a) @ 5.1 GHz; (b) @ 6.84 GHz; (c) @ 10 GHz; (d) @ 12.6 GHz.

3.5. MIMO Antenna Surface Current Distribution

To verify metamaterial role and low inter-antenna coupling, we analyze antenna surface current distribution. We select surface current distributions at four frequency points: 5.1 GHz, 6.84 GHz, 10 GHz, and 12.6 GHz. In the simulation environment, we excite antenna port 1 while connecting ports 2, 3, and 4 to a matched 50-ohm load. This allows studying antenna units 2, 3, and 4 under unit 1 interference with decoupling structure influence. Figure 11 shows that surface currents at these frequency points mainly concentrate on the radiating patch and metamaterial, while other patches show very weak surface currents. Therefore, isolation between antenna units is very high. This also demonstrates that the metamaterial structure applied in this design has broadband decoupling characteristics and good decoupling effect within the 4.66–15.97 GHz operating frequency band.

3.6. MIMO Antenna Gain and Efficiency

Figure 12 shows antenna gain and radiation efficiency curves across the entire operating frequency band. The figure reveals

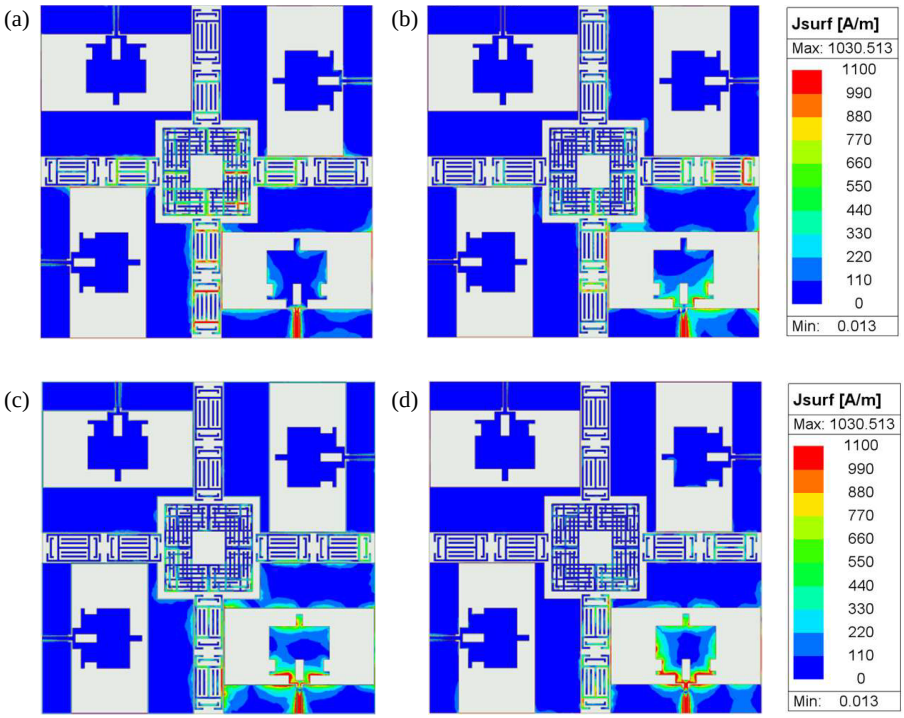

FIGURE 11. Surface current map: (a) @ 5.1 GHz; (b) @ 6.84 GHz; (c) @ 10 GHz; (d) @ 12.6 GHz.

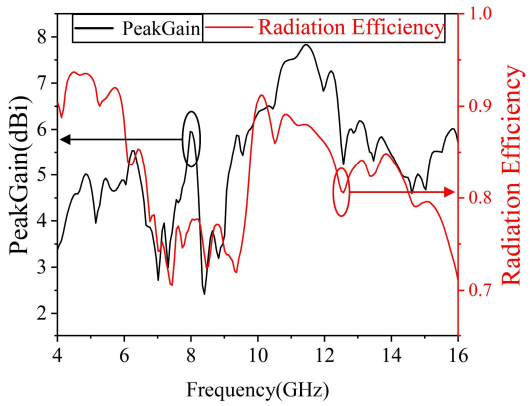

FIGURE 12. Gain and efficiency of the proposed antenna.

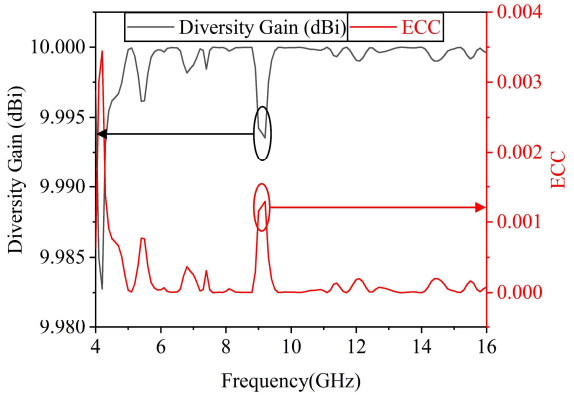

FIGURE 13. The ECC and the diversity gain value.

that antenna gain ranges 2.5–7.83 dBi from 4.66 to 15.97 GHz. Maximum antenna gain reaches 7.83 dBi at 11.45 GHz. Antenna radiation efficiency across the entire working band ranges between 70% and 94%. This indicates that most feed source energy is radiated by the antenna. The antenna demonstrates considerable gain and radiation efficiency across the entire operating frequency band, confirming good radiation characteristics.

3.7. The Diversity Characteristics of MIMO Antenna

MIMO antenna performance evaluation also requires diversity performance assessment. These evaluation metrics include envelope correlation coefficient (ECC) and diversity gain (DG). ECC is a critical antenna performance evaluation metric. We can clearly observe communication channel isolation and correlation from ECC values. Lower ECC indicates lower mutual coupling and can be recognized by a safety threshold of 1. Smaller ECC values mean antenna units work individually with less interference to other units while being more efficient. To ensure MIMO antenna operational reliability, ECC values usually need to remain below 0.05. DG serves as a MIMO antenna diversity effectiveness index. We can derive it from the antenna's ECC value, noting that ECC values range between 0 and 1. We can calculate ECC using the following equation:

$$\mathrm{ECC} = \frac{\left|S_{11}^{*}S_{12}^{'} + S_{21}^{*}S_{22}^{'}\right|^{2}}{\left(1-\left(|S_{11}|^{2}+|S_{21}|^{2}\right)\right)\left(1-\left(|S_{22}|^{2}+|S_{12}|^{2}\right)\right)}, \tag{13}$$

Figure 13 shows simulated ECC and DG values for this antenna.

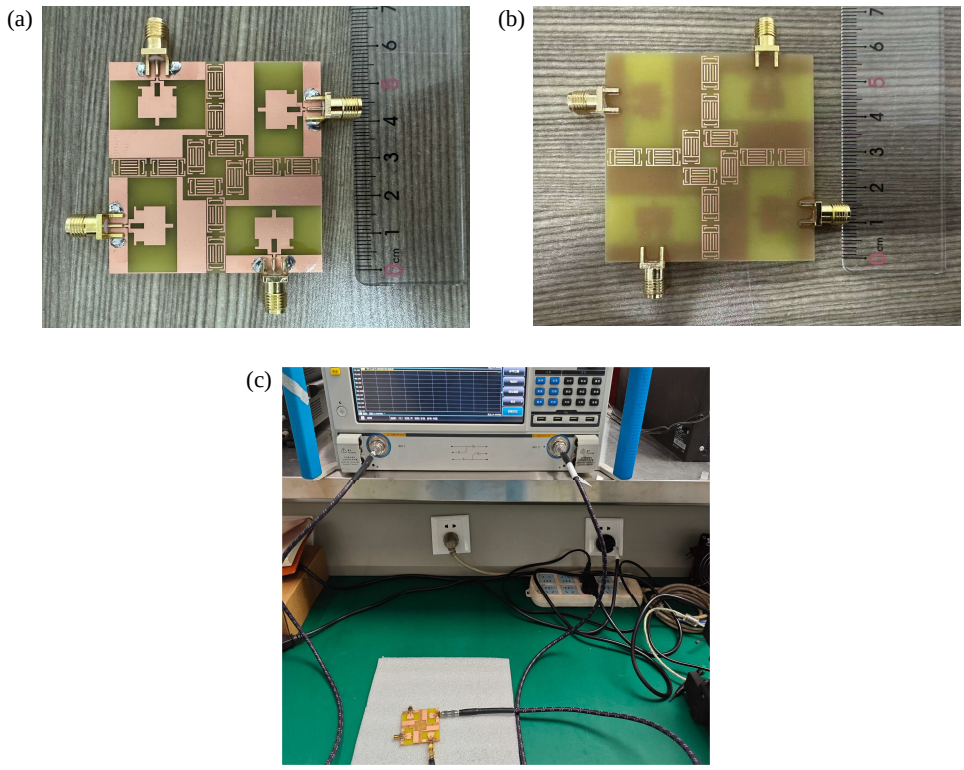

FIGURE 14. Physical processing diagram. (a) Front view, (b) back view, (c) measurement setup.

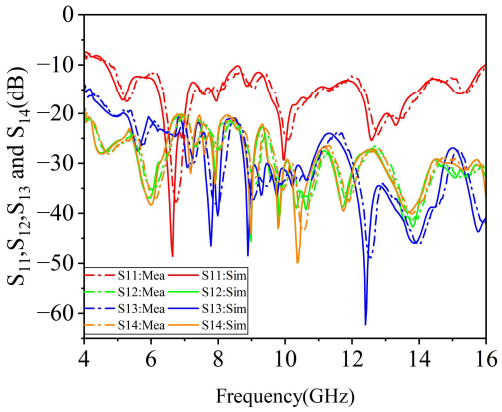

FIGURE 15. Measured and simulated values of the S-parameters.

We can observe communication channel isolation and correlation from ECC values. Lower ECC indicates lower mutual coupling. In this paper, ECC is less than 0.0035, confirming good antenna isolation.

DG is another fundamental MIMO antenna characterization parameter. It measures MIMO antenna spatial diversity. Greater diversity gain indicates better improvement in MIMO antenna technique score diversity. We can derive diversity gain calculation from the following equation:

$$\mathrm{DG} = 10 * \sqrt{1 - |\mathrm{ECC}|}, \tag{14}$$

In this paper, diversity gain DG exceeds 9.984, confirming good spatial diversity characteristics.

3.8. MIMO Antenna Physical Testing Analysis

To validate the proposed design, we fabricated and tested a prototype antenna. We fabricated the antenna using an FR4 dielectric substrate with a dielectric constant of 4.4, dielectric loss tangent of 0.02, and thickness of 1.6 mm. Given the antenna's high-frequency operating band, we strictly controlled substrate manufacturing tolerances to prevent performance degradation: thickness tolerance ± 0.05 mm, dielectric constant tolerance ± 0.1, and surface flatness tolerance ≤ 0.02 mm/m. The four antenna elements' CPW transmission lines extend from radiating patch edges to substrate side edges. We vertically soldered SMA connectors to transmission line ends on substrate side edges, ensuring deviation-free feed signal transmission.

Figure 14 shows the fabricated antenna based on these parameters. We used an Agilent Network Analyzer (VNA) to measure antenna S-parameters. Figure 15 shows measured and simulated S-parameter values.

This paper's physical measurement uncertainties mainly originate from three aspects. First, hardware losses and assembly errors can cause slight deviations between measured and simulated gain values. Second, test environment interference — anechoic chamber background noise and incomplete electromagnetic shielding — interferes with antenna radiation signal collection. Third, measurement equipment accuracy limitations — Agilent Network Analyzer calibration accuracy inconsistencies. However, these factors' impact is relatively small. Measured results align with simulated ones, antenna performance is stable, and errors remain within engineering application acceptable ranges. Results show that the pro-

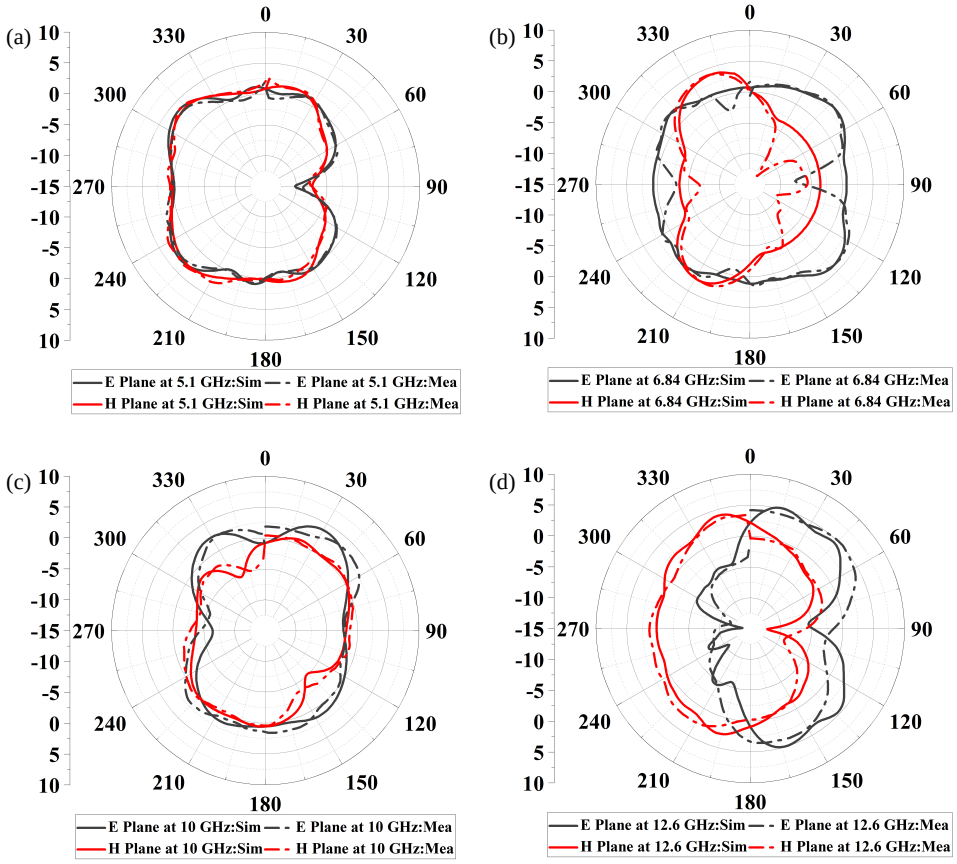

FIGURE 16. Measured and simulated radiation patterns: (a) @ 5.1 GHz, (b) @ 6.84 GHz, (c) @ 10 GHz, (d) @ 12.6 GHz.

TABLE 4. Comparison between the proposed antenna and other antennas.

Reference	Size (mm)	Bandwidth (GHz)	Isolation (dB)	Ports number	ECC	Peak Gain (dBi)	Diversity Gain (dBi)
[5]	$140 * 70 * 1.6$	6.4–7.1	18	4	0.025	6.4	NG*
[6]	$20 * 30 * 1.6$	3.01–12.34	22	2	0.0025	5.5	9.99
[7]	$36 * 27 * 1.6$	12.1–13.99	18.8	2	0.004	6.65	9.98
[10]	$75 * 75 * 1.6$	3.5–3.8	30	4	0.002	4.8	9.95
[11]	$54 * 54 * 1.6$	3–11	15	4	0.02	2.83	NG*
[12]	$40 * 24 * 1.6$	3.1–10.9	15	2	0.2	5	NG*
[13]	$50 * 28 * 1.6$	2.8–11.5	18	2	0.05	NG*	9.94
[14]	$70 * 150 * 1.6$	2.5–3.6	15	8	0.02	NG*	NG*
[15]	$55 * 26 * 1.6$	3.1–12.3	20	2	0.12	4	NG*
[16]	$95 * 60 * 1.6$	2.4–4.5	18	2	0.15	NG*	NG*
[17]	$91 * 38 * 1.6$	2.8–10	22	2	0.05	6	NG*
This work	$55 * 55 * 1.6$	4.66–15.97	20	4	0.0035	7.83	9.995

posed MIMO antenna operates from 4.66 to 15.97 GHz with $S_{11} < -10$ dB and S_{12}, S_{13}, $S_{14} < -20$ dB.

Figure 16 shows simulated and measured radiation patterns at 5.1 GHz, 6.84 GHz, 10 GHz, and 12.6 GHz frequencies, indicating that antenna far-field radiation characteristics meet requirements.

4. DISCUSSION

Table 4 compares this paper's MIMO antenna design with other papers' MIMO antenna designs. The comparison covers antenna size, operating bandwidth, number of ports, isolation, ECC (from simulation experiments), and antenna gain. Com-

pared to [7, 11–13], this paper's antenna design demonstrates higher isolation, higher gain, and wider bandwidth. Compared to [5, 10, 14–17], this paper's antenna is smaller and has wider bandwidth. Table data shows that this paper's antenna design outperforms previous antenna designs across all parameters.

5. CONCLUSIONS

This paper proposes an ultra-wideband antenna based on a coplanar waveguide structure. The antenna unit demonstrates good impedance matching with $S_{11} < -15$ dB from 4.67–14.22 GHz. This paper also proposes a novel metamaterial with good decoupling characteristics from 4.66–15.97 GHz. Finally, we design a 4-port ultra-wideband MIMO antenna comprising four antenna units based on the proposed antenna units. It achieves 11.31 GHz operating bandwidth with $S_{11} < -10$ dB from 4.66–15.97 GHz. By combining with the proposed metamaterials, we reduce the coupling between antenna units, ultimately achieving S_{12}, S_{13}, and S_{14} all < -20 dB across the operating bandwidth. This realizes ultra-wideband decoupling and high-gain radiation characteristics of 7.83 dBi.

Therefore, this paper's antenna design features not only a novel and simple structure, but also highlights metamaterial structure novelty and application innovation and flexibility. It demonstrates good performance in ultra-wideband, low-coupling, high-gain, high-radiation efficiency, and omnidirectional radiation. This antenna suits miniaturized satellites. Its simple structure facilitates integration into space-limited devices, while its ultra-wideband characteristic enables compatibility with different satellite communication frequency bands (e.g., parts of C-band, X-band, and Ku-band). Additionally, its low coupling and high gain ensure stable satellite-to-ground data transmission in complex space electromagnetic environments.

Meanwhile, this antenna architecture also has potential for expansion to higher-frequency band systems (e.g., millimeter-wave) or multi-antenna arrays, and can extend to fields like 5G ultra-wideband and vehicle-mounted radar. For millimeter-wave expansion: CPW structure and metamaterial decoupling principle are adaptable, and miniaturized metamaterials can still suppress coupling, but material optimization is necessary to reduce losses and improve processing accuracy. For multi-antenna array expansion: modular design supports unit replication, and double-layer metamaterial scheme can be reused, but algorithm optimization is necessary to reduce computational complexity and supplement signal synchronization design.

REFERENCES

[1] Alsaab, N. and M. Shaban, "Design and realization of a multi-band, high-gain, and high-isolation MIMO antenna for 5G mmWave communications," *Applied Sciences*, Vol. 15, No. 12, 6857, 2025.

[2] Khan, O., S. Khan, S. N. K. Marwat, N. Gohar, M. Bilal, and M. Dalarsson, "A novel densely packed 4×4 MIMO antenna design for UWB wireless applications," *Sensors*, Vol. 23, No. 21, 8888, 2023.

[3] Savcı, H. S., "A four element stringray-shaped MIMO antenna system for UWB applications," *Micromachines*, Vol. 14, No. 10, 1944, 2023.

[4] Chutchavong, V., W. Chanwattanapong, N. Wongsin, P. Rakluea, M. Tangjitjetsada, C. Rakluea, C. Mahatthanajatuphat, and P. Akkaraekthalin, "A flexible and compact UWB MIMO antenna with dual-band-notched double U-shaped slot on Mylar® polyester film," *Electronics*, Vol. 14, No. 17, 3363, 2025.

[5] Ghiat, A., J. R. Pérez, R. P. Torres, A. Tribak, and J. Terhzaz, "A multiple-input multiple-output antenna with metamaterial enhancement for 5G channel sounding in the upper 6 GHz band," *Electronics*, Vol. 14, No. 7, 1339, 2025.

[6] Tighilt, Y., C. Bensid, D. Sayad, S. Mekki, R. Zegadi, M. L. Bouknia, I. Elfergani, P. Singh, J. Rodriguez, and C. Zebiri, "Low-profile UWB-MIMO antenna system with enhanced isolation using parasitic elements and metamaterial integration," *Electronics*, Vol. 12, No. 23, 4852, 2023.

[7] Zheng, X., Z. Zhao, Y. Zhang, T. Zhang, A. Gui, and H. Wu, "A low-coupling broadband MIMO array antenna design for Ku-band based on metamaterials," *Journal of Electromagnetic Engineering and Science*, Vol. 24, No. 6, 666–673, 2024.

[8] Zheng, X., Z. Zhao, Y. Pan, and T. Zhang, "Design of a miniaturized symmetrical E-shaped MIMO antenna with low coupling," *Applied Computational Electromagnetics Society Journal*, Vol. 39, No. 12, 1051–1058, 2024.

[9] Ramanathan, K., S. Gopalakrishnan, and T. Chandrakanthan, "Miniaturized dual and quad port MIMO antenna variants featuring elevated diversity performance for UWB and 5G-midband applications," *Micromachines*, Vol. 16, No. 6, 716, 2025.

[10] Khan, A. A., Z. Wang, D. Li, A. Aburas, A. Ahmed, and A. Aburas, "Metamaterial-enhanced MIMO antenna for multi-operator ORAN indoor base stations in 5G sub-6 GHz band," *Applied Sciences*, Vol. 15, No. 13, 7406, 2025.

[11] Chen, L.-Y., W.-S. Zhou, J.-S. Hong, and M. Amin, "A compact eight-port CPW-fed UWB MIMO antenna with band-notched characteristic," *Applied Computational Electromagnetics Society Journal (ACES)*, Vol. 35, No. 8, 887–892, 2020.

[12] Alsath, M. G. N. and M. Kanagasabai, "Compact UWB monopole antenna for automotive communications," *IEEE Transactions on Antennas and Propagation*, Vol. 63, No. 9, 4204–4208, 2015.

[13] Ibrahim, A. A., J. Machac, and R. M. Shubair, "Compact UWB MIMO antenna with pattern diversity and band rejection characteristics," *Microwave and Optical Technology Letters*, Vol. 59, No. 6, 1460–1464, 2017.

[14] Abdullah, M., S. H. Kiani, and A. Iqbal, "Eight element multiple-input multiple-output (MIMO) antenna for 5G mobile applications," *IEEE Access*, Vol. 7, 134 488–134 495, 2019.

[15] Toktas, A. and A. Akdagli, "Compact multiple-input multiple-output antenna with low correlation for ultra-wide-band applications," *IET Microwaves, Antennas & Propagation*, Vol. 9, No. 8, 822–829, 2015.

[16] Wu, Y.-T. and Q.-X. Chu, "Dual-band multiple input multiple output antenna with slitted ground," *IET Microwaves, Antennas & Propagation*, Vol. 8, No. 13, 1007–1013, 2014.

[17] Jusoh, M., M. F. Bin Jamlos, M. R. Kamarudin, and M. F. Bin Abd Malek, "A MIMO antenna design challenges for UWB application," *Progress In Electromagnetics Research B*, Vol. 36, 357–371, 2012.

[18] Battaglia, G. M., G. G. Bellizzi, A. F. Morabito, G. Sorbello, and T. Isernia, "A general effective approach to the synthesis of shaped beams for arbitrary fixed-geometry arrays," *Journal of Electromagnetic Waves and Applications*, Vol. 33, No. 18, 2404–2422, 2019.

[19] Thotakura, H., R. Gogineni, K. S. Rao, C. K. Kumar, R. B. Sadineni, and S. Mandava, "A miniaturized highly isolated two port triple band-notched UWB MIMO antenna verified by characteristic mode analysis," *Progress In Electromagnetics Research C*, Vol. 160, 133–142, 2025.

[20] Salman, L. A. and K. M. Gatea, "Highly-miniaturized broadband MIMO antennas for WLAN/WiMAX/5G and UWB communications," *Progress In Electromagnetics Research B*, Vol. 115, 120–133, 2025.

[21] El Tayeb, M. M., D. A. El Hamid Salem, A. R. Mahmoud, I. M. Ibrahim, A. J. A. Al-Gburi, and M. H. M. Mahmoud, "A compact 4-ports UWB MIMO antenna with WiMAX and WLAN band rejection characteristics," *Progress In Electromagnetics Research C*, Vol. 160, 9–19, 2025.